



# Friction stir welding of a rapidly solidified thin-strip continuous cast AA5182 Al–Mg alloy: analysis of microstructure evolution, mechanical properties, and corrosion resistance

Hesam Pouraliakbar<sup>1</sup> · Hamed Jamshidi Aval<sup>2</sup> · Ramezanali Farajollahi<sup>2</sup> · Andrew Howells<sup>3</sup> · Mark Gallerneault<sup>4</sup> · Vahid Fallah<sup>1</sup>

Received: 9 February 2024 / Accepted: 12 June 2024 / Published online: 19 June 2024  
© The Author(s), under exclusive licence to Springer-Verlag London Ltd., part of Springer Nature 2024

## Abstract

This research explores the evolution of microstructure, mechanical properties, and resistance to corrosion in friction stir welds (FSW) of rapidly solidified continuously cast thin-strip (TS) AA5182 Al–Mg alloy. The same FSW procedures were applied to direct chill (DC) cast alloy samples of similar chemical composition with rolled and annealed microstructures to provide a basis for comparison. This study investigates the effect of the initial microstructure and manufacturing process on the weld characteristics. The findings indicate that performing FSW on annealed DC samples with a pin rotational speed of 400 rpm and a traverse speed of 160 mm/min results in the largest stir zone area (27.3 mm<sup>2</sup>) and grain size (20.4 ± 3.1 μm). The results highlight the significant impact of temperature during FSW on the grain size within the stir zone. The combined influence of heat generation and severe plastic deformation during FSW leads to the development of a random crystallographic texture in the stir zone of AA5182 alloy specimens. In contrast to the as-cast TS and as-rolled DC samples, applying FSW to the annealed DC sample induces the formation of the β-Al<sub>3</sub>Mg<sub>2</sub> phase within the stir zone. Moreover, the formation of finer equiaxed grains in the stir zone of the TS sample contributes to an increased hardness compared to the base metal. The study concludes that conducting FSW on the as-cast TS AA5182 alloy sample yields the most favorable combination of hardness, strength, and corrosion resistance when compared to both as-rolled and annealed DC AA5182 alloy samples. Furthermore, it is emphasized that microstructural changes have a more pronounced impact on the corrosion behavior of Al–Mg alloys than the residual stress generated by FSW.

**Keywords** Friction stir welding (FSW) · AA5182 Al–Mg alloy · Rapid solidification · Thin strip casting · Microstructure · Mechanical properties · Corrosion resistance

## 1 Introduction

Despite the advantages such as low density and excellent ductility, aluminum alloys have not completely replaced other alloys (e.g., steels), and they are still seeking further application in the transportation industry. However, given the growing environmental concerns among vehicle manufacturers and the pursuit of greater fuel efficiency, the trend of substituting alloys with aluminum alloys is expected to continue [1, 2]. In the transportation sector, two commonly used groups of aluminum alloys are the Al–Mg non-heat-treatable alloys (i.e., the AA5xxx series) and Al–Mg–Si heat-treatable alloys (i.e., the AA6xxx series). The overall cost of heat treatment makes it more challenging to achieve the reduction in the production costs of AA6xxx series alloys, i.e., via process optimization. In contrast, the AA5xxx series

✉ Hesam Pouraliakbar  
h.pouraliakbar@queensu.ca

✉ Hamed Jamshidi Aval  
h.jamshidi@nit.ac.ir

<sup>1</sup> Azar Advanced Manufacturing Laboratory (AAML),  
Department of Mechanical and Materials Engineering,  
Queen's University, Kingston, ON K7L 3N6, Canada

<sup>2</sup> Department of Materials Engineering, Babol  
Noshirvani University of Technology, Shariati Avenue,  
Babol 47148-71167, Iran

<sup>3</sup> Hazelett-CASTechnology, 800 Innovation Dr, Kingston,  
ON K7K 7E7, Canada

<sup>4</sup> Department of Mechanical and Materials Engineering,  
Queen's University, Kingston, ON K7L 3N6, Canada

alloys can offer a more cost-effective means of increasing the usage of aluminum alloys in the automotive and other transportation industries especially when the as-formed surface finish requirement is not as high. AA5xxx alloys possess a favorable combination of attributes, including adequate ductility, weldability, corrosion resistance, and high strength, and hold significant potential for applications in the transportation sector [2–6].

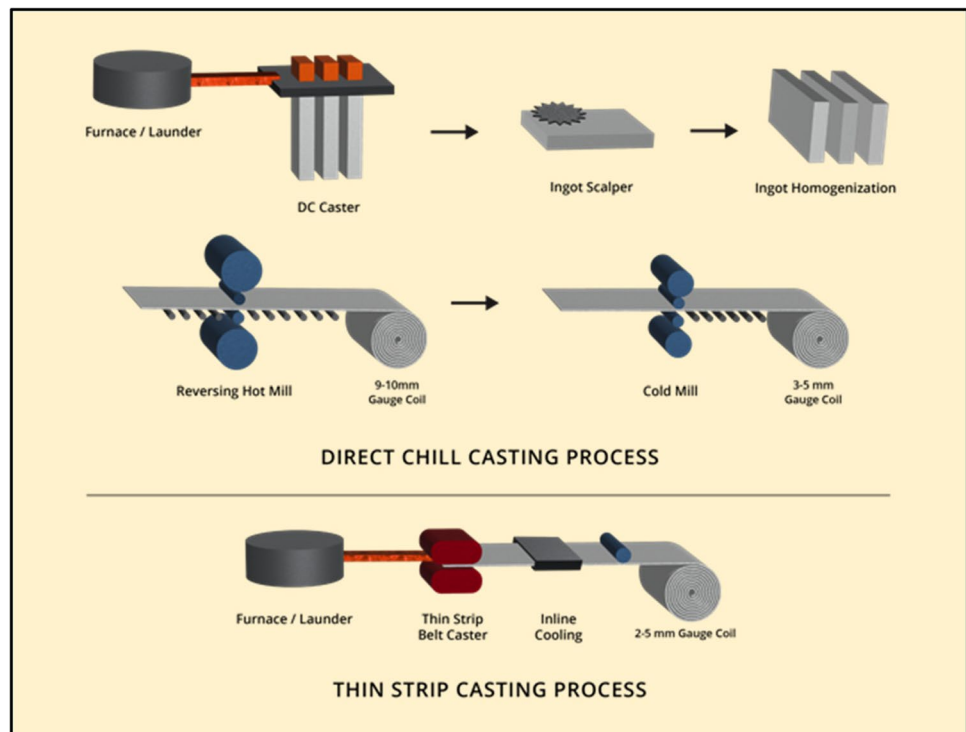
Numerous researchers and manufacturers are currently exploring innovative approaches to reduce production costs and enhance the production efficiency of aluminum alloy sheets. Recently, Hazelett-CASTechnology™ is developing a novel casting process called thin strip (TS) casting, which allows for the continuous casting of aluminum strips with thicknesses ranging from 2 to 5 mm. This new TS casting method, with correspondingly faster cooling than that of conventional direct chill (DC) casting, has the potential to revolutionize the production of thin aluminum strips [7–9]. This is an energy-efficient and cost-effective approach wherein a thin layer of molten metal flows between two counter-rotating cooling belts, solidifying rapidly and uniformly [9, 10]. Figure 1 illustrates the schematic production routes for both the TS and DC casting, comparing the two methods. As can be seen from the figure, the TS casting eliminates the need for intermediate processing steps of “scalping,” “homogenization,” and “hot rolling,” as well as a significant portion of the final “cold rolling” stage, commonly employed in traditional casting techniques such as DC casting [7, 8]. This results in a significantly shorter

production line for the final sheet products. It is well understood that the reduced melt thickness in continuous casting, leads to higher quenching rates, and typically results in a finer microstructure, decreased solute microsegregation, and ultimately a higher solute supersaturation within the matrix [10–12].

Welding is often an unavoidable step in the fabrication process within the transportation industry, and it is crucial to thoroughly investigate how its input parameters affect newly developed alloys [7, 13, 14]. Meanwhile, as an environmentally friendly solid-state welding technique, friction stir welding (FSW) stands as a viable option for joining TS AA5182 strips. Unlike sheets fabricated through the DC method, which undergo a series of thermomechanical processing steps, the strips produced via TS casting exhibit a rapidly solidified cast structure. Consequently, the microstructure development and, therefore, the mechanical properties in the TS sheets differ from those in DC. Accordingly, the behavior of the TS sheets during welding may differ significantly from that of the conventional DC sheets, thereby necessitating an investigation into the differences.

Several researchers have investigated the FSW of AA5xxx series Al–Mg alloy sheets [7, 15–21]. Bagheri Hariri et al. [22] explored how rotational and traverse speed affected the mechanical properties and corrosion behavior of FSWed AA5052. They observed that increasing the welding traverse speed from 200 to 250 mm/min improved mechanical properties and corrosion resistance and contributed to the formation of a fine-grained structure and a

**Fig. 1** The schematic representation of the TS and DC casting routes. The innovative TS production line is shortened by eliminating intermediate production steps [8]



more pronounced passive film. Kwon et al. [23] delved into the FSW of annealed AA5052 alloys and found that reducing rotational speed increased the hardness and strength of the stir zone. At 500 rpm rotational speed and 100 mm/min traverse speed, the average hardness of the stir zone was 33% higher than that of the base metal. Saravana Kumar and Rajasekaran [24] investigated the underwater FSW of AA5083, noting that the ultimate tensile strength of the joint increased up to 191 MPa due to the high cooling rate. Yoon et al. [25] studied the impact of welding parameters on the microstructure and mechanical properties of O-temper AA5052. Their findings revealed that increasing the traverse speed and decreasing the rotational speed led to a reduction in the stir zone grain size while enhancing the hardness and strength of the joint. Hattingh et al. [26] explored the influence of tool geometry on the required welding force and joint strength in AA5083. They found that optimizing the geometry and using threaded conical pins with vertical grooves could achieve a joint strength equivalent to 95–97% of the base metal strength. Hirata et al. [27] investigated the effect of heat input on the microstructure and ductility of FSWed AA5083-O. They concluded that increasing the tool's rotational speed to traverse speed ratio decreased joint strength and ductility while causing coarsening of the structure in the stir zone. Chen et al. [28] examined the impact of tool angle on the formation of various defects in FSW of AA5456, finding that the tool angle significantly influenced the heat input, affecting material flow and leading to defects formation in the stir zone. Leitao et al. [29] focused on the mechanical properties of AA5182, noting the relationship between the thermomechanically affected zone (TMAZ) and weld strength, the grain size in the TMAZ influenced the weld properties. Lombard et al. [30] explored how tool rotational and traverse speeds affected the residual stress in FSWed AA5083. They found that increasing heat input expanded the area under tensile residual stress in joints. Peel et al. [31] demonstrated that longitudinal residual stresses in FSW of AA5083 increased with tool traverse speed due to the formation of more temperature gradients. Sato et al. [32] investigated the FSW of AA5052, revealing that the maximum fracture strain occurred when the stir zone contained grains ~ 10  $\mu\text{m}$  in size, and a decrease in fracture strain was observed in grain sizes larger or smaller than 10  $\mu\text{m}$ . Torzewski et al. [33] studied the microstructure and fatigue properties of FSWed AA5083 alloys, finding that forming fine recrystallized grains in the stir zone increased hardness, and

stress concentration at the heat-affected zone of FSW joints could act as a fatigue crack initiator.

In the existing literature, a substantial portion of the research pertaining to AA5xxx alloys revolves around dissimilar welding involving these alloys and other aluminum alloy series such as AA1xxx, AA2xxx, and AA6xxx, or alloys containing various alloying systems. These studies primarily emphasize the occurrence of defects and mechanical properties [14, 30–32, 34, 35], with a focus on wrought Al–Mg alloys. Conventional casting techniques produce ingots that need to be thermomechanically processed into sheets suitable for welding. In contrast, this study introduces the innovative TS casting method, which directly produces cast strips ready for welding, eliminating the need for intermediate processing steps. Up to this point, a thorough assessment of the characteristics of TS AA5182 Al–Mg strip welds has been lacking. Recognizing the importance of understanding the microstructure and mechanical behavior of these sheets during welding, this study marks the first comparison of the microstructure evolution and mechanical properties of FSWed TS AA5182 sheet with those of as-rolled, as well as annealed, counterparts fabricated via the conventional DC casting route. Furthermore, this investigation examines the impact of the welding process on the corrosion resistance and residual stress development of the welded samples.

## 2 Experimental procedure

In this research, samples of TS AA5182 measuring 10  $\times$  15  $\text{cm}^2$  with a thickness of 3 mm were used. For comparison, as-rolled and as-annealed DC AA5182 specimens were subjected to FSW alongside the as-cast TS samples. The chemical composition of the employed sheets, listed in Table 1, indicates that both samples possess comparable chemical compositions, with solute contents falling within the acceptable range for AA5182 alloy [9]. Full-penetration butt joining of the sheets using FSW was performed along the length of the cut samples by a H13 steel tool with a 3–5-mm square-side frustum probe and an 18 mm shoulder diameter with conical geometry. The pin length was 2.8 mm, and the plunging depth was 0.2 mm. The applied pin design is represented schematically in Fig. 2. A K-type thermocouple is inserted in the joint line to control the temperature during welding. The thermocouple was inserted

**Table 1** Examined chemical composition for TS and DC AA5182 samples

Sample type	Chemical composition (wt%)				
	Al	Mg	Mn	Fe	Si
TS AA5182	Bal	4.38 $\pm$ 0.01	0.23 $\pm$ 0.002	0.11 $\pm$ 0.001	0.04 $\pm$ 0.004
DC AA5182	Bal	4.51 $\pm$ 0.03	0.42 $\pm$ 0.005	0.17 $\pm$ 0.003	0.09 $\pm$ 0.001

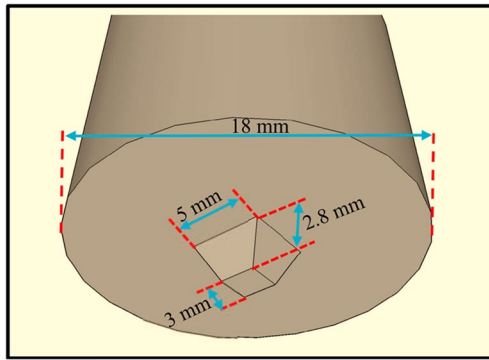


**Fig. 2** The schematic depiction of the H13 tool employed for FSW of AA5182 sheet specimens

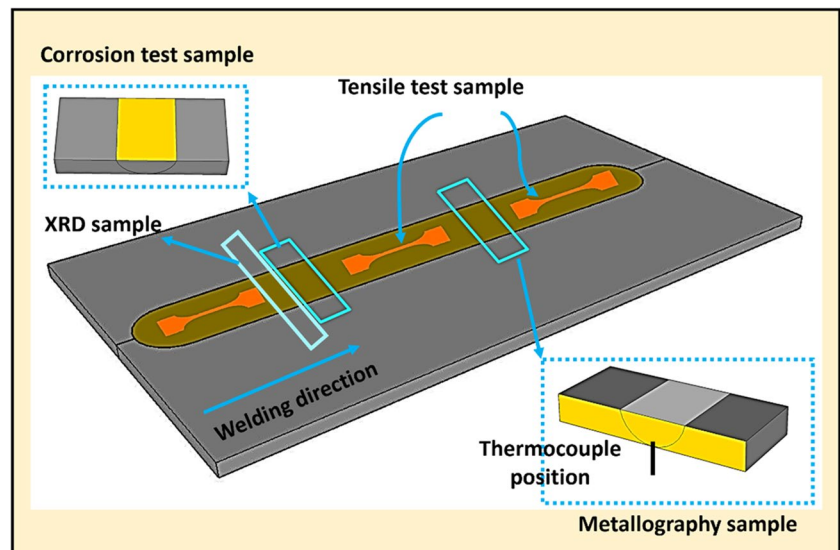
through the fixture's designated hole from the underside of the joining sheets. To precisely record the equilibrium temperature, the thermocouple made direct contact with the weld (i.e., the stir zone) and was positioned halfway along the pin traverse path (i.e., the length of the weld line). The location of the thermocouple is indicated in Fig. 3. Welding was performed with a 400 rpm pin rotation and 160 mm/min traverse speed. Table 2 presents how the specimens are labeled in this study. The rolled DC sheet was annealed at 350 °C for 4 h before welding to investigate the effect of the annealed microstructure of the base metal on the properties of the weld. Various samples were extracted to study the microstructure, mechanical properties, corrosion resistance, and residual stress, as shown in Fig. 3. The metallographic samples were etched after mechanical grinding and polishing using a modified Poulton solution and examined under an optical microscope (OM) and scanning electron microscope (SEM) equipped with an X-ray energy dispersive spectrometer (EDS). The joint cross-section was subjected

**Table 2** The labeling of base metals and welded specimens in this study

Specimen label	Rotational speed (rpm)	Traverse speed (mm/min)	Treatment condition
TS	-	-	As-cast TS sheet
DC	-	-	As-rolled DC sheet
DC-O	-	-	Annealed DC sheet
W-TS	400	160	Welded as-cast TS sheet
W-DC	400	160	Welded as-rolled DC sheet
W-DC-O	400	160	Welded annealed DC sheet

to microhardness tests. Microhardness was measured following ASTM E92 standard [36] with a load of 100 g and a dwell time of 15 s. The ambient temperature tensile tests were carried out according to the ASTM E8 standard [37] on an STM-250 universal testing machine under the fixed crosshead speed regime at 1 mm/min speed. At least, three different specimens machined along the welding line were examined. The tensile samples were taken from the stir zone along the weld line and the width of the tensile samples conformed entirely to the stir zone according to ASTM E8 standards while any thinning of the thickness due to flash formation had no impact on the tensile samples. The longitudinal residual stress of welded samples was measured using the X-ray diffraction (XRD) technique with Cu-K $\alpha$  radiation in the direction perpendicular to the welding line according to ASTM E915 standard [38]. Analysis was conducted at seven distinct points, each spaced 10 mm apart on either side of the weld line, with the midpoint of the weld serving as the reference point. Residual stress measurements

**Fig. 3** Illustration of the sampling locations for experimental specimens, including tensile testing, corrosion testing, XRD, and metallography on the welded samples. The areas highlighted in yellow indicate the specific zones where the respective tests were conducted





and XRD data were acquired from the upper surface of the experimental samples. When subjected to either tensile or compressive forces, the interplanar spacing (denoted as “ $d$ ”) experiences alterations, expanding, or contracting as a result of the applied tension or compression. This change in the distance between crystallographic planes at a fixed wavelength will appear as a shift in the position of the diffraction peak ( $\Delta\theta$ ), according to Bragg’s equation [39] and the definition of strain:

$$\varepsilon = \frac{d - d_0}{d_0} = -\cot\theta\Delta\theta \quad (1)$$

where “ $d_0$ ” is the interplanar spacing in the state of no strain for the diffractive plane, “ $d$ ” is the interplanar spacing under strain, and “ $\theta$ ” is the diffraction angle. For calculation of the stress tensor (i.e., normal stresses including  $\sigma_{xx}$ ,  $\sigma_{yy}$ , and  $\sigma_{zz}$ ), it is necessary to calculate the normal strains (i.e.,  $\varepsilon_{xx}$ ,  $\varepsilon_{yy}$ , and  $\varepsilon_{zz}$ ) which can be obtained from Eq. (1). The following equation provides the value of the stress component along the  $x$ -axis (i.e., welding direction):

$$\sigma_{xx} = \frac{E}{(1 + \nu)(1 - 2\nu)} [(1 - \nu)\varepsilon_{xx} + \nu(\varepsilon_{yy} + \varepsilon_{zz})] \quad (2)$$

where “ $E$ ” is Young’s modulus and “ $\nu$ ” is Poisson’s ratio ( $\sim 0.3$ ). The corrosion resistance of samples was evaluated using a potentiodynamic polarization test in 3.5 wt.% NaCl solution as the corrosion medium. All samples were polarized at 25 °C at a scanning rate of 1 mV/s and corrosion tests were conducted on the stir zone surface as depicted in Fig. 3.

### 3 Results and discussion

In Fig. 4, a cross-sectional view of various welding samples is presented. The temperatures recorded by thermocouples at the weld lines of the W-TS, W-DC, and W-DC-O samples, all subjected to the same FSW parameters, were 387 °C, 370 °C, and 401 °C, respectively. Additionally, based on cross-sectional image analysis of the joints (averaged over at least three sections for each sample), the stir zone dimensions for these samples were 24.1 mm<sup>2</sup>, 25.4 mm<sup>2</sup>, and 27.3 mm<sup>2</sup>, respectively. The measurement of the stir zone dimensions revealed that, as the stir zone temperature increases, the area of the stir zone also increases. As stated by Mofarreh et al. [40], higher temperatures lead to reduced material flow stress, facilitating plastic deformation, and consequently, the expansion of the stir zone. Since the process parameters and tool geometry were the same for all three samples, the temperature disparity can be attributed to the inherent differences in the sheets, including their microstructure. This distinction results in varying thermomechanical behaviors. Notably, the W-DC-O sample exhibits the highest

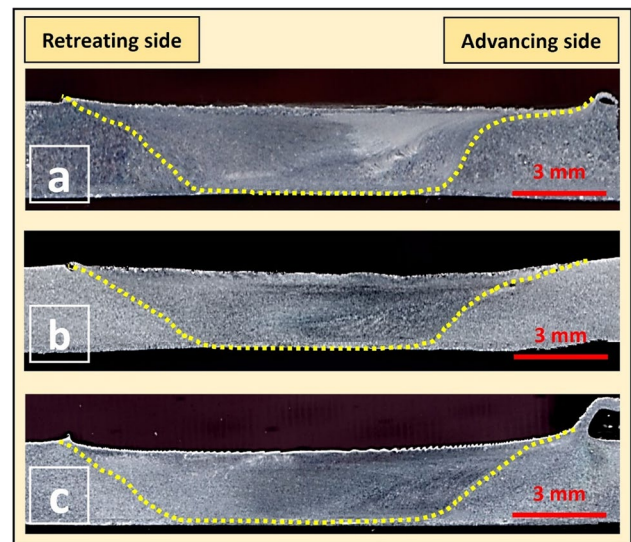
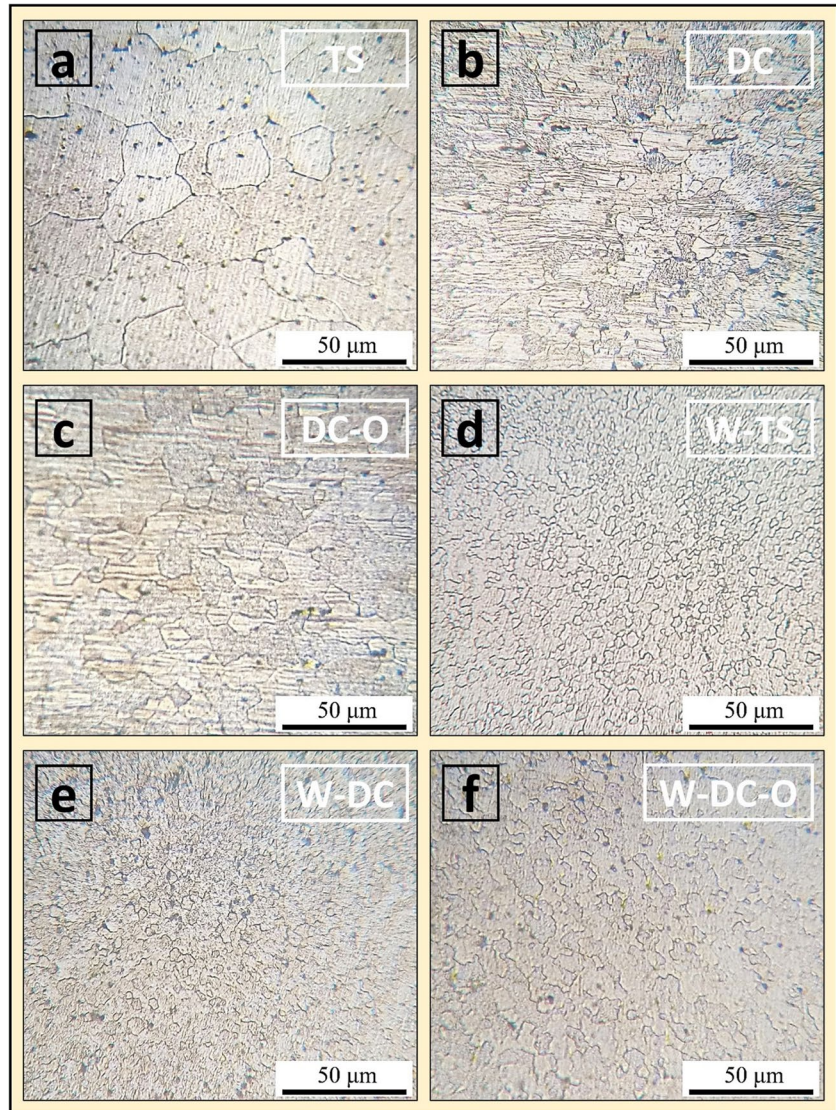


Fig. 4 The cross-section of different weld samples: a W-TS, b W-DC, and c W-DC-O

temperature in its weld, indicating a greater contribution from heat generated due to friction and plastic deformation in this specific sample. Since the flow stress of AA5xxx aluminum alloys in the annealed state is less than that in the work-hardened state [41], it is anticipated that the heat generated by plastic deformation would increase during FSW when the material is annealed. Also, the as-cast TS AA5182 sheet exhibited a higher temperature rise upon welding than the as-rolled DC sample, attributed to its lower yield strength (YS), i.e., 112.7 vs. 324.6 MPa, respectively. Consequently, the elevated temperature observed in the annealed DC sample (i.e., W-DC-O) is attributed to a lower flow stress during the thermomechanical process involved in welding.

Figure 5 shows OM images of the microstructures of the base metals, including the as-cast TS, as-rolled DC, and annealed DC samples, as well as the stir zones of various weld samples, namely W-TS, W-DC, and W-DC-O samples. The base metals, TS, DC, and DC-O, exhibit grain sizes of approximately  $43.2 \pm 4.1$ ,  $26.5 \pm 3.8$ , and  $36.4 \pm 2.9$   $\mu\text{m}$ , respectively. In contrast, the stir zone grain size in W-TS, W-DC, and W-DC-O samples is approximately  $16.9 \pm 2.7$ ,  $10.8 \pm 2.9$ , and  $20.4 \pm 3.1$   $\mu\text{m}$ , respectively. Notably, variations in the stir zone grain size do not appear to have a straightforward correlation with the grain size of the base metal. As suggested in the literature [42], temperature and plastic strain have opposing impacts on the formation of the recrystallized microstructure in the stir zone, i.e., a higher temperature promotes grain growth and thus a larger grain size, whereas a higher plastic strain and/or strain rate promotes nucleation of grains and therefore a finer grain size evolution. In accordance with Chang et al. [43], the following equation describes the plastic strain rate during FSW:

**Fig. 5** OM images of base metals and stir zones of different weld samples: **a** as-cast TS sample, **b** as-rolled DC sample, **c** annealed DC sample, **d** sample W-TS stir zone, **e** sample W-DC stir zone, and **f** sample W-DC-O stir zone



$$\dot{\epsilon} = \frac{\omega\pi w}{D} \quad (3)$$

where, “ $\omega$ ” is the rotational speed (rpm), and “ $D$ ” and “ $w$ ” represent the depth (mm) and width (mm) of the stirred zone, respectively.

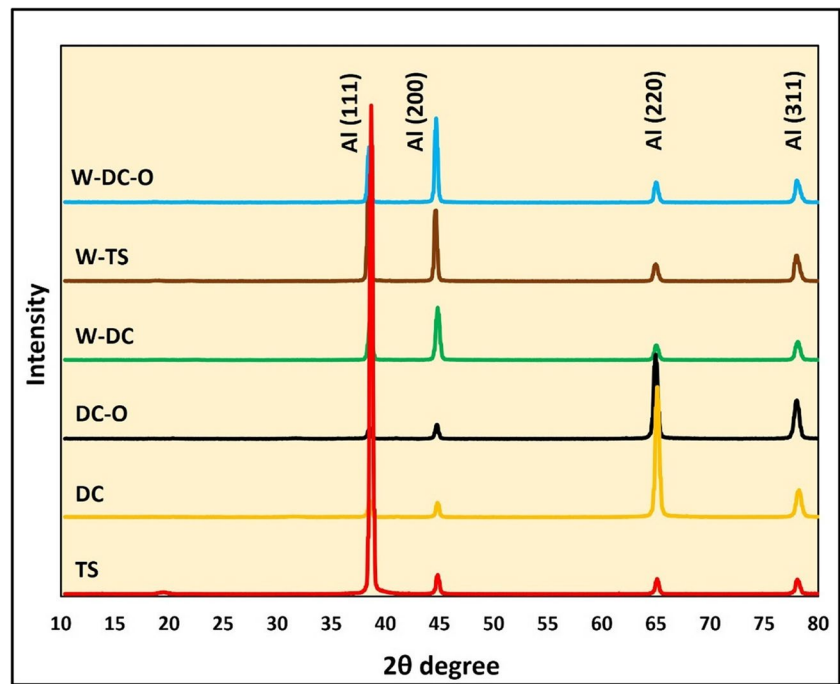
When comparing the dimensions of the stir zones in the W-TS, W-DC, and W-DC-O samples, it was evident that the annealed sample experiences a greater plastic strain rate and thus plastic strain by applying a constant welding traverse speed. Therefore, the larger grain size in this sample suggests that the effect of temperature on stir zone grain growth has dominated that of plastic strain in promoting grain nucleation. On the other hand, despite the lower plastic strain, the W-DC sample exhibits a finer grain size in the stir zone, indicating limited grain growth due to its lower processing temperature. For the W-TS sample, its grain size falls between the other two samples and so does its temperature,

thereby indicating the dominant role of temperature in its grain size evolution. Thus, in all three samples, the stir zone temperature appears to be the dominant factor controlling the grain size evolution.

Figure 6 displays the XRD patterns obtained from all fabricated samples. XRD patterns of the weld samples acquired from the stir zone surface according to Fig. 3. Apart from the prominent peaks associated with the aluminum matrix, no other peaks are discernible in the samples. This observation suggests that the volume fraction of secondary phase particles in the microstructure is low. The rapidly solidified TS sample’s pattern exhibits a pronounced preferred orientation compared to the DC and DC-O samples, i.e., the presence of a strong (111) peak. However, following the FSW process, the diffraction intensities of different crystallographic planes show no significant variations across the samples. This phenomenon, as per the findings of other researchers [44, 45], is attributed to the influence of thermomechanical processing,



**Fig. 6** The examined XRD patterns for different samples



the change of preferred texture in the base metal, and the development of a random texture in the welded samples. To assess and compare the samples, the texture parameter ( $TP_{hkl}$ ) was calculated using the method outlined by Dickson [46] based on the examined XRD patterns, as plotted in Fig. 7. The  $TP_{hkl}$  was estimated as follows [47]:

$$TP_{hkl} = \frac{I_{hkl}}{I_{0hkl}} \quad (4)$$

$$= \frac{1}{n} \sum_{i=1}^n \frac{I_{hkl}}{I_{0hkl}}$$

where the “ $I_{hkl}$ ” is the intensity of a specific crystallographic plane. To calculate the corresponding  $TP_{hkl}$ , four significant reflections of the  $\alpha$ -Al including (111), (200), (220), and (311) were employed. There are no notable distinctions in  $TP_{hkl}$  among all the welded samples. Given the formation of random texture in the welded samples, there is no prevailing crystallographic orientation that could impact the mechanical properties and corrosion resistance of these samples. Figure 8 presents SEM images of various samples. As indicated by the results of the EDS analysis, the microstructure of the base metals consists of intergranular eutectic  $\beta$ - $Al_3Mg_2$  and intermetallic Al-(Mn,Fe) secondary phase particles. In Fig. 8, these phases are denoted as #1 (i.e.,  $\beta$ -phase) and #2 (i.e., Al-(Mn,Fe) phase) and are highlighted by arrows. While the morphology of these particles exhibits slight variations in the TS, DC, and DC-O base metals, the chemical composition of these phases is somehow consistent. It is worth noting that the SEM images were acquired from the central region of the strip thickness, considering that the TS sample possesses a thru-thickness gradient

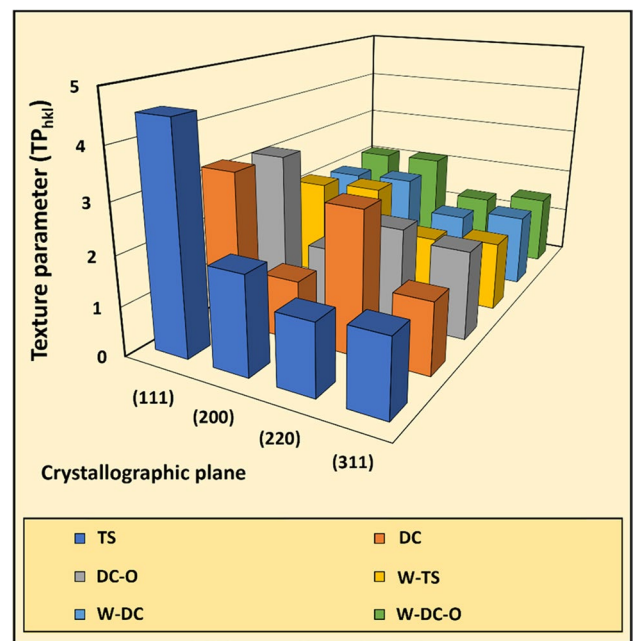
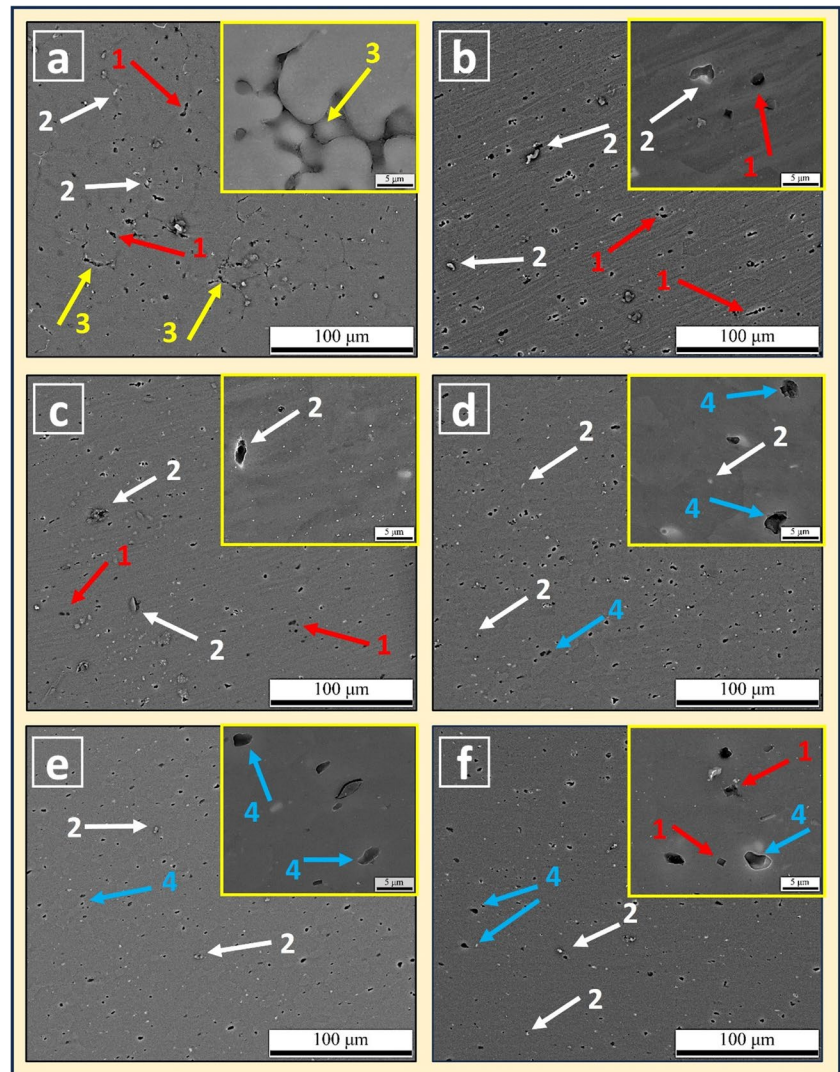


**Fig. 7** The calculated  $TP_{hkl}$  for different samples based on XRD patterns given in Fig. 6

structure in which the particle and grain size increase by moving away from the strip surfaces. More details on the microstructure evolution in TS and DC alloys can be found in the principal author’s recent studies [7–9]. As reported in that research, the formation of shrinkage porosity in the central regions of the TS strip occurs due to an insufficient flow of melt to fill the gap between solidification fronts (from the

**Fig. 8** SEM images showing the microstructure of base metals and stir zones in weld samples: **a** as-cast TS sample, **b** as-rolled DC sample, **c** annealed DC sample, **d** sample W-TS stir zone, **e** sample W-DC stir zone, and **f** sample W-DC-O stir zone



top and bottom belts) during the final stages of solidification. This region is labeled as #3 and only appears in Fig. 8a.

Based on the EDS analysis, the increased Si content in the Al-(Mn,Fe) intermetallic particles of the DC-O sample indicates that this phase (i.e., Al-(Mn,Fe)-Si particles) becomes enriched during annealing. This enrichment is either absent or negligible in the as-cast TS and as-rolled DC base metals. Following welding, the stir zone of the W-TS, W-DC, and W-DC-O samples contains Al-(Mn,Fe)-Si and  $Mg_2Si$  particles (i.e., labeled as #4 in Fig. 8), replacing the initial Al-(Mn,Fe) particles and  $\beta$ -phase. This suggests that the generation of heat and the applied plastic deformation during the FSW process facilitate Si diffusion within the aluminum matrix, enabling the formation of Al-(Fe,Mn)-Si and  $Mg_2Si$  particles. Figure 9 shows typical EDS analysis results for  $\beta$ -phase, Al-(Mn,Fe)-Si and  $Mg_2Si$  phases in the weld metals. However, there is no evidence of  $\beta$ -phase in the stir zones of W-TS and W-DC samples. In contrast, the  $\beta$ -phase with polyhedral morphology appears in the microstructure

of the W-DC-O sample. In the W-DC-O sample, this phase dissolves in the aluminum matrix due to the frictional heat and severe plastic deformation caused by FSW. The dissolution of the Mg-rich  $\beta$ -phase elevates the solute concentration within the aluminum in the weld metal, contributing to solid solution strengthening. However, the conditions for the re-precipitation of the  $\beta$ -phase are provided only in the W-DC-O sample due to the higher temperatures reached during FSW. The increased peak temperature in the stir zone enables atomistic diffusion, which is typically slow or even impossible when the activation energy provided by frictional heat is low. Due to the increased supersaturation in the solid solution (caused by the dissolution), the system thermodynamically aims to decrease its free energy by forming small polyhedral  $\beta$ -phase particles, re-precipitating from the aluminum solid solution. Due to the typically higher cooling rates in small welds than in larger-scale processes such as casting, it is kinetically more feasible to form fine, solute-concentrated zones or precipitates within the matrix



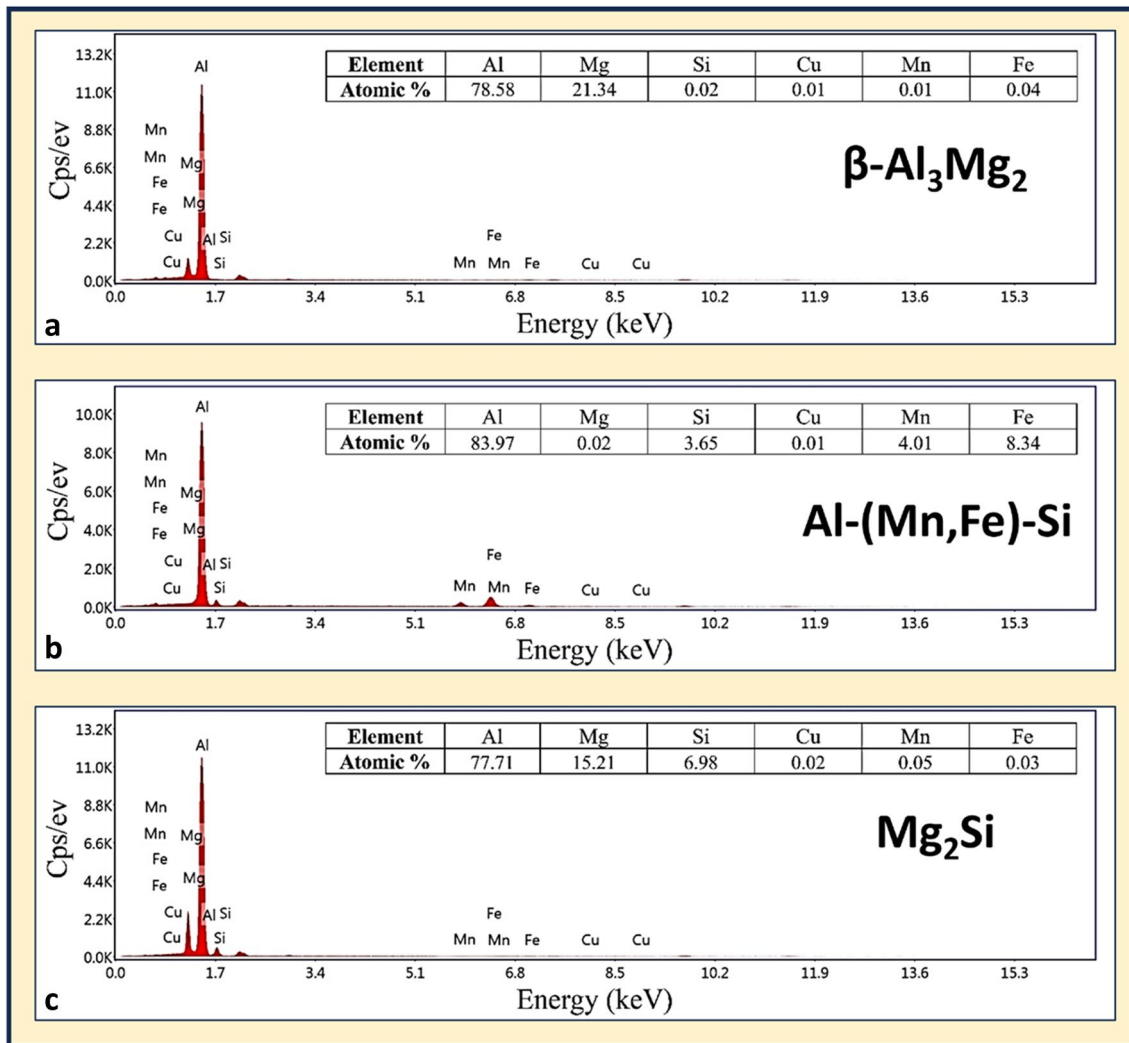


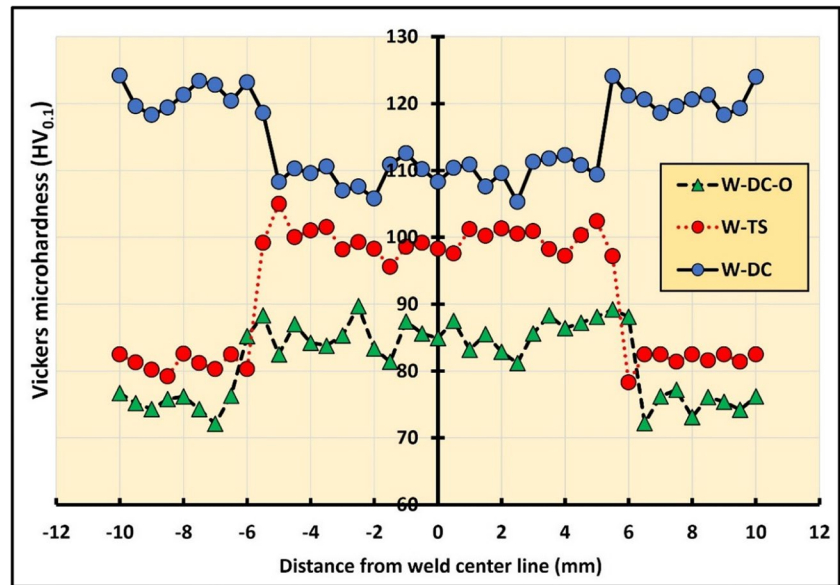
**Fig. 9** Typical SEM–EDS spectra and analysis results obtained for different phases in the stir zone of weld samples: **a**  $\beta$ -phase, **b** Al-(Mn,Fe)-Si, and **c** Mg<sub>2</sub>Si

(specifically in the stir zone) rather than promoting diffusions over longer distances to encourage particle growth. A similar phenomenon was also observed in a recent study by the authors [7] where it was found that re-precipitation of polyhedral intergranular  $\beta$ -phase particles occurred in the stir zone of samples subjected to higher rotational speeds (e.g., 800–1200 rpm) and slower traverse speeds (e.g., 40 mm/min). This revealed that a higher heat input during welding leads to increased re-precipitation of initially dissolved  $\beta$ -phase with a polyhedral morphology at the grain boundaries of dynamically recrystallized equiaxed grains in the stir zone. The formation of intergranular Mg-rich  $\beta$ -phase has been reported to sensitize and enhance the corrosion susceptibility of samples [48–50].

Figure 10 illustrates the microhardness profiles obtained from various weld samples. While the hardness within the stir zone remains relatively unaltered consistently across

different samples, the overall pattern of microhardness variation differs. In the W-DC-O sample, the stir zone's hardness has increased compared to the base metal. This phenomenon can be attributed to the formation of a fine, equiaxed dynamically recrystallized microstructure, in contrast to the coarse grains present in the base metal, resulting in increased hardness as per the Hall-Patch relationship [51]. Conversely, the hardness of the weld metal in the W-DC sample has decreased with respect to the base metal. Even though the stir zone in this sample exhibits a higher hardness than the other samples due to its smaller grain size, the release of a high amount of stored energy in the as-rolled state (i.e., strain release and reduction in dislocation density) resulting from the influence of frictional heat during FSW led to a lower hardness than in the base metal. This decrease in hardness of the weld metal could not be fully compensated for by the higher solute content (i.e., resulting from the dissolution

**Fig. 10** The examined microhardness profile of different weld samples



of the  $\beta$ -phase), which contributes to the strengthening of the aluminum matrix in the weld metal. The hardness of the W-TS sample has increased in comparison to the base metal. This increase is due to the formation of a finer, equiaxed microstructure in the stir zone, as well as solid solution strengthening resulting from a higher solute concentration (i.e., mainly Mg content) due to the dissolution of the initial  $\beta$ -phase. However, it is important to note that the hardness value is lower than that of the as-rolled DC sample implying the prevailing effect of work hardening by higher dislocation density over solid solution strengthening by solute supersaturation. Considering the associated mechanisms in hardness and comparing the distribution patterns illustrated in Fig. 10 shows that the most substantial difference in hardness between the base metal and weld metal was observed in the as-cast TS sample, with values of  $81 \pm 2$  and  $98 \pm 3$  HV<sub>0.1</sub>, respectively. In contrast, the annealed DC sample displayed the least significant difference in average hardness, with values of  $73 \pm 2$  and  $85 \pm 2$  HV<sub>0.1</sub>, respectively.

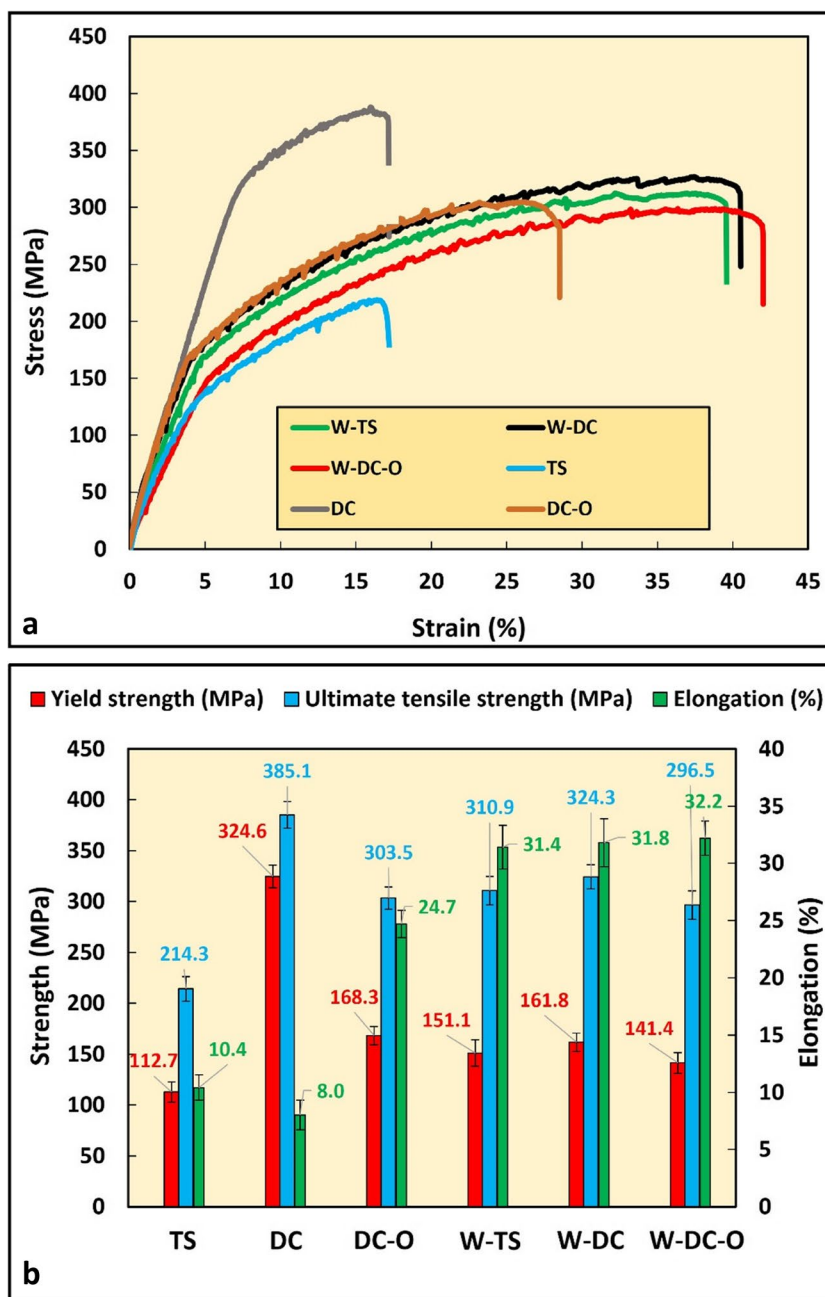
Figure 11 displays the engineering stress–strain curves obtained from tensile tests on various samples. To ensure the reliability of the results, three tensile specimens were tested for each condition, and the one that best represents the average properties is shown for each sample type. The Portevin–Le Chatelier (PLC) effect is evident in both base metal and welded samples, indicative of dynamic strain aging (DSA) resulting from the dynamic interaction of mobile dislocations and solutes (primarily Mg in AA5182 alloy) [7–9]. Although the base metals exhibit significantly different mechanical characteristics, the welded samples show no significant variations in terms of strength and ductility. This can be attributed to the thermomechanical processes occurring during the FSW, which lead to substantial refinement of

grains and second-phase particles. These processes largely eliminate the distinctions in the initial microstructure of the base metals employed. The minor differences observed in the properties presented in Fig. 11 can be ascribed to variations in grain size and the types of particles formed in the stir zone of these samples. Notably, the finer microstructure developed in the stir zone of the W-DC sample has a tangible impact by increasing both YS and UTS. Furthermore, the larger grain size and, therefore, coarser intergranular particles in the stir zone of the W-DC-O sample contribute to a higher elongation.

Figure 12 illustrates the fracture surfaces of various samples. All samples exhibit abundant dimples on their fracture surfaces, indicating a ductile fracture nature. In addition to the dimple formation, the fracture surface of the TS base metal shows some intergranular separation, attributed to centerline porosity (Fig. 12a). It is worth noting that, due to the refinement and evolution of microstructure, there is no evidence of intergranular separation after welding in the W-TS sample (Fig. 12d). This indicates that the entire centerline porosity region was healed through the flow of plasticized metal during FSW. Another significant observation is that, in the W-DC-O sample with higher elongation, the depth and size of the dimples have increased (Fig. 12f).

Several mechanisms contribute to enhancing the strength of the stir zone effectively. One key factor influencing the strength of the welded samples is the reinforcement provided by the grain boundaries. In line with the Hall–Petch equation [52], strength increases with the reduction in grain size due to the increase in grain boundary area. The smaller grain size observed in sample W-DC suggests that this mechanism has a more pronounced effect in this sample compared to the others. Additionally, solid solution strengthening is

**Fig. 11 a** Examined engineering stress–strain curve and **b** average tensile properties of samples



another mechanism at play, where the dissolution of alloying elements like Mg serves to strengthen the aluminum matrix. The level of Mg dissolved in the aluminum matrix (i.e., referred to as solute supersaturation) decreases with the re-precipitation of the  $\beta$ -phase. Consequently, in the case of the W-DC-O sample, where re-precipitation of Mg-rich  $\beta$ -phase occurs, it is expected that this mechanism’s contribution to strengthening will not be as significant as in the other samples. Considering that the size of the second-phase particles falls within the micron range, the Orowan strengthening mechanism is not likely to be effective in the stir zones of these samples.

Figure 13 demonstrates the profile of residual stresses in various samples. The pattern of changes in residual stresses is consistent across the three welded samples: within the stir zone and regions close to the weld line, the residual stress exhibits a tensile nature, while it transitions to a compressive nature further away from the weld line. However, we note that the tensile stress within the weld centerline is lower than that in the areas outside the stir zone. Residual stresses develop in welds because of the uneven temperature changes experienced during welding. When materials are welded together, they are subjected to intense heat followed by quick cooling. This rapid thermal cycle results in uneven



**Fig. 12** SEM images captured from the tensile fractured surface of base metals and weld samples: **a** as-cast TS base metal, **b** as-rolled DC base metal, **c** annealed DC base metal, **d** sample W-TS stir zone, **e** sample W-DC stir zone, and **f** sample W-DC-O stir zone

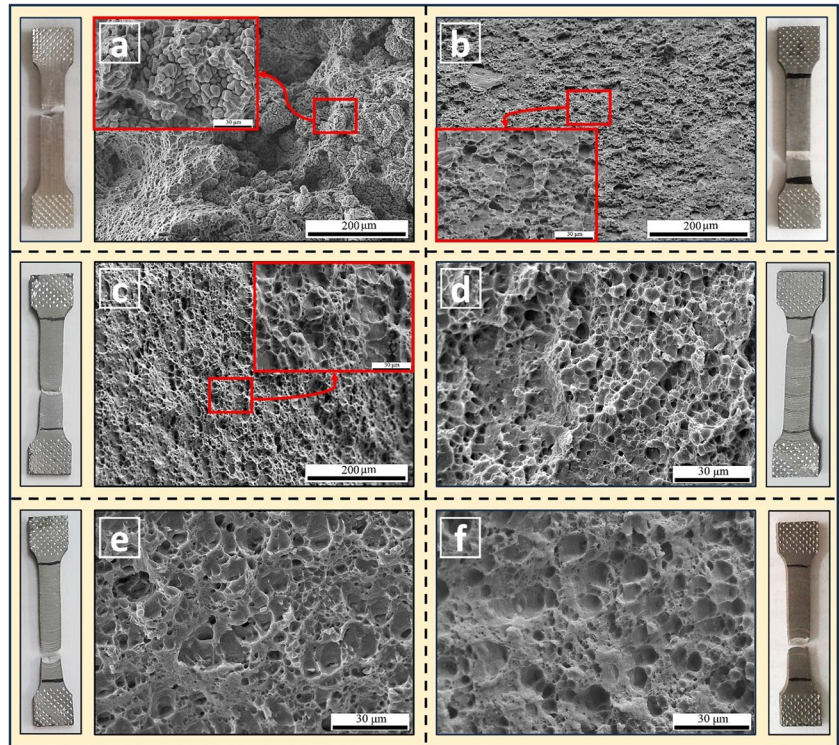
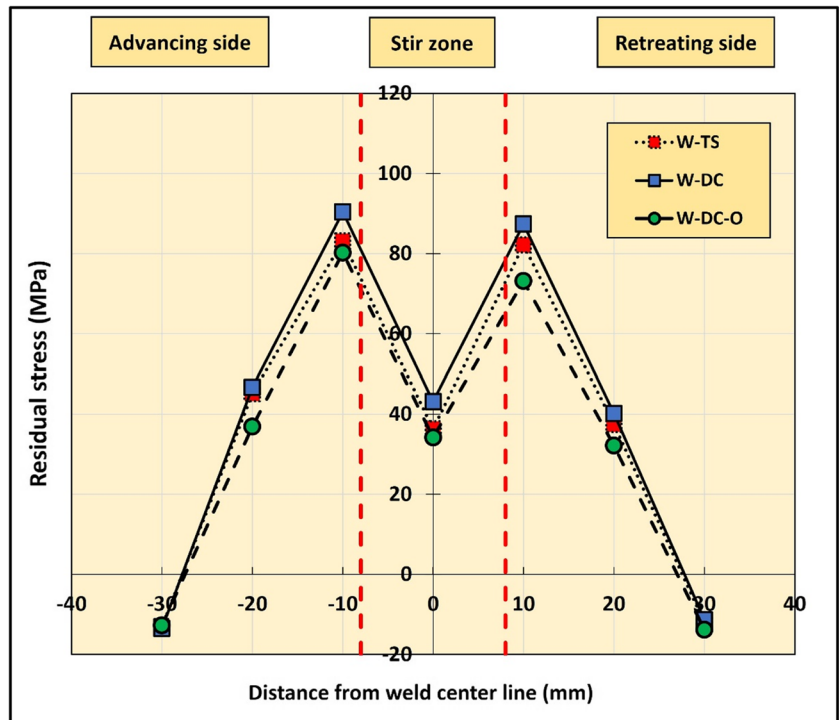


**Fig. 13** The longitudinal residual stress ( $\epsilon_{xx}$ ) profile of different weld samples



expansion and contraction of the material, which creates residual stresses. Besides, other factors including metallurgical changes (such as phase transformations and grain growth), restricted thermal expansion, joint configuration, welding parameters, and material characteristics (such as

yield strength and hardness) also play a role in generating residual stresses in welds [53–55]. In addition, the formation of residual stresses in the welded joints is the outcome of the interplay between the microstructure and the thermo-mechanical history during welding [56]. Both tensile and

compressive residual stress components can indeed form simultaneously in a weld. Tensile thermal stresses build up as the weld center line, which experiences higher temperatures, undergoes contraction upon cooling down. Consequently, tensile residual stresses develop at the center line towards the end of the cooling process. Furthermore, the compressive plastic stress/strain generated in the stir zone, by pushing the plasticized material backward, alleviates a portion of the tensile residual stresses.

The balance between tensile and compressive residual stresses depends on various factors such as welding parameters, joint geometry, material properties, and post-weld cooling processes. Meanwhile, as the material undergoes softening and plastic deformation within the stir zone during FSW, along with the rise in temperature altering the characteristics of the plasticized material, some of the tensile residual stresses are relieved. This alteration impacts the equilibrium between stress components, leading to a decrease in the tensile residual stress depicted in Fig. 13. Ultimately, in areas away from the welded region, the compressive residual stresses dominate the tensile stresses from the weld. Other studies [31, 57–59] have reported similar residual stress patterns to those found in this study. The magnitude of the tensile residual stress increases with the base metal strength. Consequently, as the mechanical restraint in the area surrounding the weld increases, the level of residual stress also rises. Similar findings correlating an increase in base metal strength and higher residual stress levels have been previously documented [60–62]. The minimum and maximum tensile residual stresses are 80.2 and 90.3 MPa in samples W-DC-O and W-DC, respectively. Based on the plotted profile, the concentration of residual stresses is slightly higher on the advancing side of all weld samples compared to the retreating side. According to the data presented in Fig. 13, the disparity in residual stresses between the advancing and retreating sides of FSW can be attributed to several factors. During FSW, the advancing side experiences greater pressure from the rotating tool, resulting in greater plastic flow compared to the retreating side. This increased plastic flow leads to more substantial material redistribution and consolidation on the advancing side, consequently yielding higher residual stresses. Additionally, variations in the geometry of the rotating tool, particularly its shoulder and pin, influence contact conditions and material deformation at both sides, potentially resulting in differing pressure levels and frictional heat generation, hence impacting residual stress distribution. Moreover, temperature gradients within the weld zone contribute to this phenomenon, with the advancing side typically subjected to higher temperatures and prolonged exposure to the heat source. These elevated temperatures affect the mechanical properties of the material and its response to plastic deformation, thereby contributing to differences in residual stress

levels. Furthermore, differences in cooling rates between the advancing and retreating sides play a role, with the retreating side cooling more rapidly due to reduced heat generation, leading to discrepancies in residual stress magnitude and distribution. In summary, the interplay of plastic flow, tool geometry, thermal effects, cooling rates, and welding parameters collectively influences the observed variations in residual stress distribution between the advancing and retreating sides of FSW welds. This higher tensile residual stress in welded samples is expected to lead to a decrease in corrosion resistance.

Polarization tests were carried out on both the base metals and the welded samples to assess their corrosion resistance. Figure 14 illustrates the polarization curves, and Table 3 presents the data concerning corrosion current, potential, and corrosion rate calculated from these tests. Additionally, Fig. 15 exhibits the corrosion products formed on the tested surfaces of the base and weld metals. It is important to highlight that, as depicted in Fig. 3, the corrosion test specimens were extracted from the weld samples within the stir zone, and thus, the outcomes of the tests solely represent the corrosion characteristics of the weld metals. The results indicate that the welded samples W-TS and W-DC exhibit lower corrosion currents and rates compared to their respective base metals, with the most significant difference observed in the case of the W-TS sample compared to the TS sample. However, sample W-DC-O displays a higher corrosion rate than its base metal. Notably, among the samples, W-TS demonstrates the highest corrosion resistance, with a 41% lower corrosion rate than the base metal (i.e., as-cast TS AA5182 alloy). Furthermore, it exhibits the least volume of corrosion products when compared to the base metal (Fig. 15 a vs. d). The corrosion resistance of aluminum alloys is significantly affected by secondary-phase particles and by grain size [48, 63]. The main driver for corrosion is the difference in electro-potential between the supersaturated aluminum matrix (i.e., the cathode in AA5182) and the  $\beta$ -phase particles (i.e., the anodes in AA5182). However, the driving force for corrosion is reversed if we consider the aluminum matrix and the Al-(Mn,Fe) particles (i.e., where the  $\beta$ -phase is absent). Thus, the matrix is the anode, and the intermetallic particles would act as cathodic sites. In any case, the size and number density of the cathodes drives corrosion. In the case of sample W-TS, the enhanced corrosion resistance of the weld metal can be primarily attributed to the breakdown of coarser Al-(Mn,Fe) intermetallic particles that act as cathodes. The absence of the  $\beta$ -phase at grain boundaries in the stir zone of sample W-TS is due to its dissolution during FSW contributes positively to its corrosion resistance. Although various results have been reported regarding the effect of both the size and electro-potential of intermetallic particles on the corrosion resistance of aluminum alloys [48, 64, 65], it should be noted that the separation of

**Fig. 14** Polarization curves obtained in 3.5 wt% NaCl solution for different samples

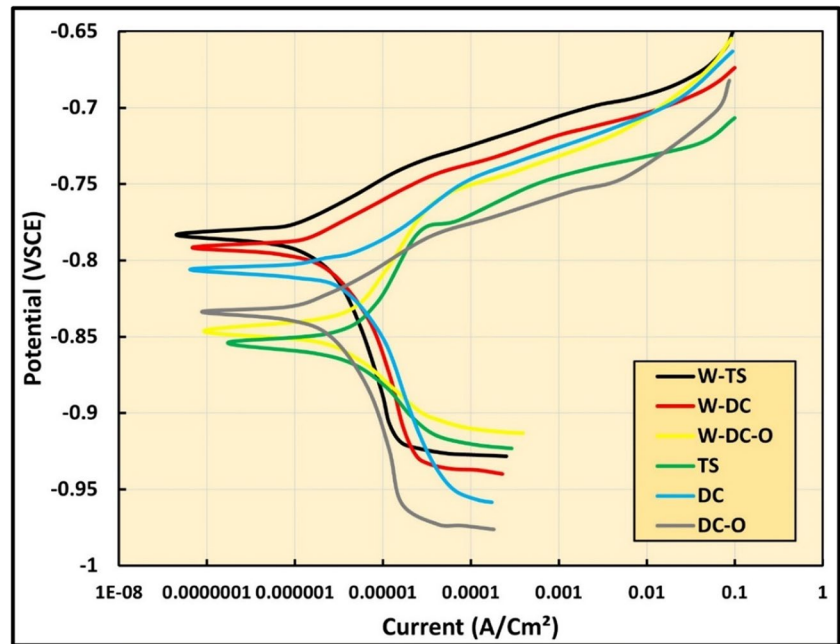


**Table 3** The values of corrosion current, potential, and rate obtained from polarization results

Sample label	$i_{\text{corr}}$ ( $\mu\text{A}\cdot\text{cm}^{-2}$ )	$E_{\text{corr}}$ (VSCE)	Corrosion rate (mm/year)
W-TS	0.34	-0.78	0.0385
W-DC	0.54	-0.79	0.0405
W-DC-O	0.73	-0.84	0.0573
TS	0.87	-0.85	0.0653
DC	0.67	-0.8	0.0432
DC-O	0.82	-0.83	0.0501

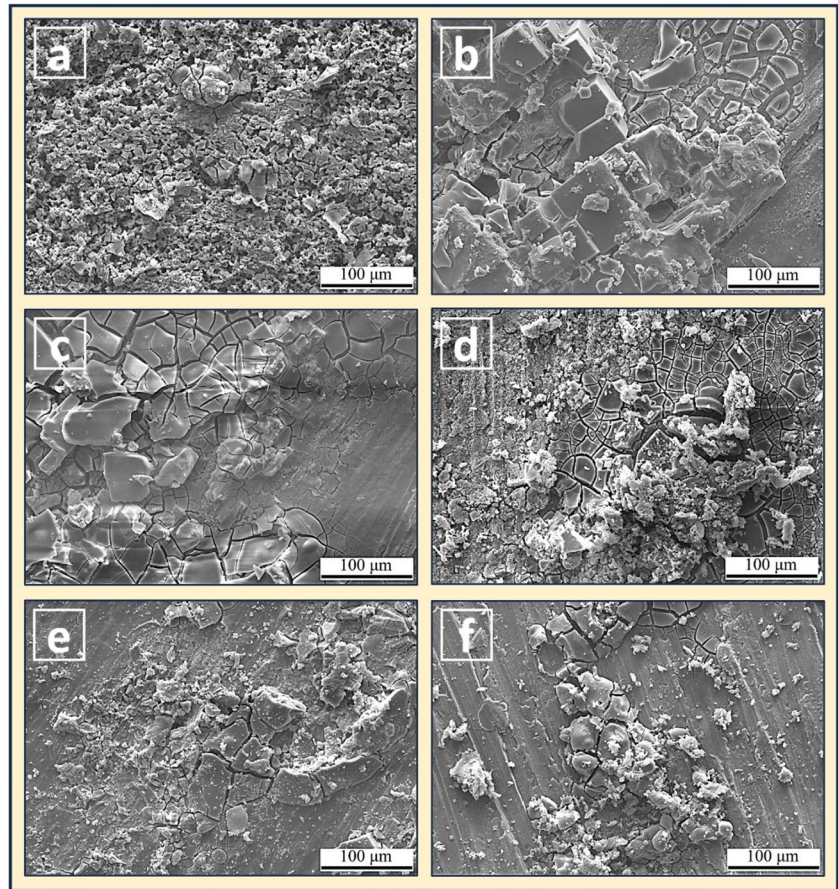
intermetallics and the formation of particles smaller than the critical size required for galvanic corrosion tend to passivate the aluminum alloy.

In addition, the formation of fine grains during the FSW accelerates the development of a thick and uniform oxide layer on the sample surface due to the application of severe plastic deformation, which can further enhance the corrosion resistance of sample W-TS after welding. Similar findings have been reported regarding the effect of severe deformation on improving the corrosion resistance of aluminum alloys [66–68]. Moreover, the corrosion resistance of sample W-DC has improved in comparison to its base metal (i.e., as-rolled DC AA5182) through the reduction in the size of second-phase particles and the dissolution of the  $\beta\text{-Al}_3\text{Mg}_2$  phase after welding. However, the higher tensile residual stress in the W-DC sample, as compared to sample W-TS, has had a negative impact on its corrosion resistance and has led to an increase in the volume of corrosion products (Fig. 15 e vs. b). Tensile and compressive residual stresses

exhibit distinct impacts on the corrosion behavior of welded samples. Tensile residual stresses, which pull the material apart, facilitate corrosion by creating preferential sites for crack initiation and propagation. Corrosive agents can infiltrate along these stress-induced cracks, accelerating corrosion. Moreover, by disrupting the protective oxide layer on the material's surface, tensile stresses induce micro-cracking and delamination of the oxide layer, exposing the underlying material to corrosive attack. Furthermore, by accelerating the breakdown of the passive film, tensile stresses promote localized corrosion, leading to increased corrosion rates. In contrast, compressive residual stresses, which push the material together, offer some beneficial effects on corrosion behavior by counteracting the impact of applied tensile stresses. In regions with compressive residual stresses, they mitigate the effect of tensile stresses, diminishing the likelihood of crack initiation and propagation. Additionally, compressive stresses uphold the integrity of the passive film on the material's surface, diminishing susceptibility to localized corrosion [69, 70]. Overall, tensile residual stresses typically exacerbate corrosion issues, whereas compressive residual stresses offer some level of defense against corrosion-related problems. Nonetheless, the precise effects of residual stresses on corrosion behavior depend on various factors such as stress magnitude, distribution, and orientation, along with environmental conditions and material properties. Sample W-DC-O, on the other hand, exhibited lower corrosion resistance compared to its base metal (i.e., annealed DC AA5182 alloy). This can be attributed to the presence of the  $\beta$ -phase, which, due to its anodic nature, exacerbates the corrosion in Al–Mg alloys [71]. Taking into account the residual stress profile and the outcomes of the



**Fig. 15** SEM images of corroded surfaces of base metals and welded samples: **a** as-cast TS base metal, **b** as-rolled DC base metal, **c** annealed DC base metal, **d** sample W-TS stir zone, **e** sample W-DC stir zone, and **f** sample W-DC-O stir zone



polarization test, it appears that evolution in the microstructure, such as grain size reduction and the formation, dissolution, and refinement of secondary-phase particles, has a more significant influence on the corrosion characteristics of Al–Mg alloys compared to the residual stress generated FSW.

## 4 Conclusions

The FSW was performed on TS and DC AA5182 Al–Mg alloy samples of similar composition having a cast, rolled, and annealed microstructure. The effects of the initial microstructure on the microstructure evolution, mechanical properties, and corrosion resistance of the weld samples were investigated. The following are the key findings:

- While FSW on the as-rolled DC AA5182 alloy produces the smallest grain size ( $10.8 \pm 2.9 \mu\text{m}$ ), there is not a clear correlation between changes in stir zone grain size and the base metal grain size. That is, the grain size of the base metal does not necessarily determine the grain size of the stir zone after FSW. This finding implies that the microstructure evolution during FSW is influenced by

various factors, such as temperature, plastic strain, and deformation rate, which can lead to the formation of a unique microstructure in the stir zone that is different from the base metal.

- The elevated temperature and plastic strain experienced during FSW of the annealed DC AA5182 alloy sheet led to the reprecipitation of the  $\beta\text{-Al}_3\text{Mg}_2$  phase in the stir zone.  $\beta$ -phase was not observed in the stir zone of as-cast TS and as-rolled DC samples. Being an intermetallic phase, the  $\beta$ -phase has the potential to influence the mechanical characteristics and corrosion resistance of the weld specimens. The emergence of the  $\beta$ -phase within the stir zone of the annealed DC sample can be attributed to the input parameters utilized during FSW, which encourage the diffusion of Mg and subsequent reprecipitation of the  $\beta$ -phase. Hence, it is imperative to account for the impact of FSW on the microstructure and attributes of the weld samples.
- Despite the stir zone's hardness ( $110 \pm 3 \text{HV}0.1$ ) in the as-rolled DC sample being higher than that of other samples, it undergoes strain softening compared to the base metal due to generated heat during FSW. The strain softening phenomenon is attributed to the release of stored energy in the form of dislocations and grain

growth, which can occur due to the high temperature and plastic deformation during FSW. Therefore, it is crucial to optimize the FSW parameters based on the initial microstructure of the base metal.

- The tensile residual stresses in the advancing side of the annealed and as-rolled DC samples range from a minimum of 80.2 MPa to a maximum of 90.3 MPa. In contrast, the as-cast TS sample falls in between these values in terms of its residual stress. The formation of residual stresses in the welded joints is the outcome of the interplay between the microstructure and the thermomechanical history during welding. The uneven and non-uniform temperature distribution along the weld line contributes to the quantity and distribution of welding residual stresses.
- Although the base metals exhibit significantly different mechanical characteristics, the welded samples show no significant variations in terms of strength and ductility. In comparison to the annealed and as-rolled DC AA5182 samples, FSW applied to the as-cast TS AA5182 sample results in the most favorable combination of hardness ( $98 \pm 3$  HV0.1), UTS ( $310.9 \pm 30.4$  MPa), and corrosion rate (0.0385 mm/year).
- The greatest corrosion resistance is observed in the weld metal of the as-cast TS AA5182 alloy, which exhibits a 41% lower corrosion rate than the base metal. Considering residual stress profiles and polarization test results, microstructure evolution, including grain size variation and the formation/dissolution of secondary-phase particles, appears to play a more substantial role in determining the corrosion behavior of Al–Mg alloys. Residual stress generated during FSW was found to be less effective in corrosion resistance in all examined specimens.

**Acknowledgements** The authors appreciate Hazelett-CASTechnology™ for their financial support and provision of resources.

**Author contribution** Hesam Pouraliakbar: formal analysis, data curation, investigation, writing—original draft. Hamed Jamshidi Aval: experimental design, methodology, investigation, writing—original draft. Ramezanali Farajollahi: investigation. Andrew Howells: formal analysis, resources, writing—review and editing. Mark Gallerneault: formal analysis, resources, writing—review and editing. Vahid Fallah: conceptualization, methodology, data curation, writing—review and editing, supervision.

**Funding** The authors received financial support from the Mitacs Accelerate Program (Grant No. IT17218).

**Data availability** No data was used for the research described in the article.

## Declarations

**Competing interests** The authors declare no competing interests.

## References

1. Kelly JC, Dai Q (2021) Life-cycle analysis of vehicle lightweighting: a review, Electric, Hybrid, and Fuel Cell Vehicles, pp 91–104
2. Roth R, Clark J, Kelkar A (2001) Automobile bodies: can aluminum be an economical alternative to steel? *JOM* 53(8):28–32
3. Fadzil M, Abdullah A, Samad Z, Yusof F, Manurung Y (2021) Application of lightweight materials toward design for sustainability in automotive component development. Elsevier, *Design for Sustainability*, pp 435–463
4. Grasserbauer J, Weißensteiner I, Falkinger G, Kremmer TM, Uggowitzer PJ, Pogatscher S (2021) Influence of Fe and Mn on the microstructure formation in 5xxx alloys—part I: evolution of primary and secondary phases. *Materials* 14:3204
5. Li YJ, Arnberg L (2004) Solidification structures and phase selection of iron-bearing eutectic particles in a DC-cast AA5182 alloy. *Acta Mater* 52(9):2673–2681
6. Zha M, Li Y, Mathiesen RH, Bjørge R, Roven HJ (2013) Annealing response of binary Al-7Mg alloy deformed by equal channel angular pressing. *Mater Sci Eng, A* 586:374–381
7. Pouraliakbar H, Jamshidi Aval H, Howells A, Gallerneault M, Fallah V (2023) Microstructural evolution and mechanical properties of rapidly solidified thin-strip continuous cast AA5182 Al-Mg alloy under varying heat inputs in friction stir welding. *Int J Adv Manuf Technol* 129(7):2921–2931
8. Pouraliakbar H, Howells A, Gallerneault M, Fallah V (2024) Anomalous mitigation in phase evolution impacting thermal stability in a rapidly solidified AA5182 Al-Mg alloy via continuous thin-strip casting. *Adv Eng Mater* 26(3):2301610
9. Pouraliakbar H, Howells A, Gallerneault M, Fallah V (2024) Fracture behavior of a rapidly solidified thin-strip continuous cast Al-Mg alloy with the Portevin-Le Chatelier effect under varying strain rates. *J Alloy Compounds* 971:172810
10. Yin S, Saidi P, Howells A, Gallerneault M, Fallah V (2023) Yield strength modelling via precipitation/recovery kinetics in rapidly solidified thin-strip cast AA6005 AlMgSi sheets subjected to cold rolling and direct aging. *Mater Sci Eng A* 888:145790
11. Wen W, Liu WC, Morris JG (2004) The effect of precipitation of Mg2Al3 and of MnAl6 on texture evolution during isothermal annealing and subsequently on formability of CC AA5182 Al alloy. *Mater Sci Eng, A* 380:191–207
12. Glenn AM, Russo SP, Paterson PJK (2003) The effect of grain refining on macrosegregation and dendrite arm spacing of direct chill cast AA5182. *Metall and Mater Trans A* 34:1513–1523
13. Ahmed MM, El-Sayed Seleman MM, Fydrych D, Çam G (2023) Çam, Friction stir welding of aluminum in the aerospace industry: the current progress and state-of-the-art review. *Materials* 16(8):2971
14. Zuiko IS, Malopheyev S, Mironov S, Kaibyshev R (2022) Dissimilar friction stir welding of AA2519 and AA5182. *Materials* 15(24):8776
15. Saravanakumar R, Rajasekaran T, Pandey C, Menaka M (2022) Mechanical and microstructural characteristics of underwater friction stir welded AA5083 armor-grade aluminum alloy joints. *J Mater Eng Perform* 31:8459–8472
16. Wang GQ, Zhao YH, Tang YY (2020) Research progress of bobbin tool friction stir welding of aluminum alloys: a review. *Acta Metallurgica Sinica (English Letters)* 33:13–29
17. Soyama H, Simoncini M, Cabibbo M (2021) Effect of cavitation peening on fatigue properties in friction stir welded aluminum alloy AA5754. *Metals* 11:59
18. Bernard D, Hattingh DG (2015) Development of high welding speed in friction stir welded 5182–H111, and the resulting influence on down force. *Mater Sci Forum* 828–829:366–373

19. MohammadiSefat M, Ghazanfari H, Blais C (2021) Friction stir welding of 5052–H18 aluminum alloy: modeling and process parameter optimization. *J Mater Eng Perform* 30:1838–1850
20. Sahu M, Paul A, Ganguly S (2022) Influence of frictional heat spread pattern on the formation of intermetallic layers at the dissimilar FSW joint interface between AA 5083 and HSLA steel. *J Manuf Process* 83:555–570
21. Chen ZW, Pasang T, Qi Y (2008) Shear flow and formation of nugget zone during friction stir welding of aluminium alloy 5083-O. *Mater Sci Eng, A* 474:312–316
22. Hariri MB, Shiri SG, Yaghoobinezhad Y, Rahvard MM (2013) The optimum combination of tool rotation rate and traveling speed for obtaining the preferable corrosion behavior and mechanical properties of friction stir welded AA5052 aluminum alloy. *Mater Des* 50:620–634
23. Yong-Jai K, Seong-Beom S, Dong-Hwan P (2009) Friction stir welding of 5052 aluminum alloy plates. *Trans Nonferrous Metals Soc China* 19:s23–s27
24. R. Saravana Kumar, T. Rajasekaran, Optimizing the underwater friction stir welding parameters to enhance the joint strength of armour grade aluminium alloy AA5083 butt joints, *Materials Today: Proceedings*, 47 (2021) 6999–7005.
25. Sung-Ook Y, Myoung-Soo K, Hyun-Bin N, Yong-Jai K, Sung-Tae H, Jin-Chun K, Kwang-Hak L, Chang-Yong L, Jong-Dock S (2012) Friction stir butt welding of A5052-O aluminum alloy plates. *Transactions of Nonferrous Metals Society of China* 22:s619–s623
26. Hattingh DG, Bignault C, Van Niekerk TI, James MN (2008) Characterization of the influences of FSW tool geometry on welding forces and weld tensile strength using an instrumented tool. *J Mater Process Technol* 203:46–57
27. Hirata T, Oguri T, Hagino H, Tanaka T, Chung SW, Takigawa Y, Higashi K, Douglas CH, Kenneth SV (2007) Influence of friction stir welding parameters on grain size and formability in 5083 aluminum alloy. *Mater Sci Eng, A* 456:344–349
28. Chen HB, Yan K, Lin T, Chen SB, Jiang CY, Zhao Y (2006) The investigation of typical welding defects for 5456 aluminum alloy friction stir welds. *Mater Sci Eng, A* 433:64–69
29. Leitao C, Leal RM, Rodrigues DM, Loureiro A, Vilaca P (2009) Mechanical behaviour of similar and dissimilar AA5182-H111 and AA6016-T4 thin friction stir welds. *Mater Des* 30:101–108
30. Lombard H, Hattingh DG, Steuwer A, James MN (2009) Effect of process parameters on the residual stresses in AA5083-H321 friction stir welds. *Mater Sci Eng, A* 501:119–124
31. Peel M, Steuwer A, Preuss M, Withers PJ (2003) Microstructure, mechanical properties and residual stresses as a function of welding speed in aluminium AA5083 friction stir welds. *Acta Mater* 51:4791–4801
32. Sato YS, Sugiura Y, Shoji Y, Park SHC, Kokawa H, Ikeda K (2004) Post-weld formability of friction stir welded Al alloy 5052. *Mater Sci Eng, A* 369:138–143
33. Torzewski J, Grzelak K, Wachowski M, Kosturek R (2020) Microstructure and low cycle fatigue properties of AA5083 H111 friction stir welded joint. *Materials* 13:2381
34. Palanivel R, Mathews PK, Murugan N, Dinaharan I (2012) Effect of tool rotational speed and pin profile on microstructure and tensile strength of dissimilar friction stir welded AA5083-H111 and AA6351-T6 aluminum alloys. *Mater Des* 40:7–16
35. Shirazi H, Kheirandish S, Pouraliakbar H (2020) Employing hooking and effective sheet thickness to achieve optimum failure load in lap joints of friction stir welded AA5456 aluminum. *Theoret Appl Fract Mech* 105:102423
36. ASTM E92-17 (2017) Standard test methods for Vickers hardness and Knoop hardness of metallic materials. ASTM International, West Conshohocken
37. ASTM International Committee E-28 on Mechanical Testing (2016) Standard test methods for tension testing of metallic materials. ASTM international
38. ASTM, E915-21 (2022) Standard practice for verifying the alignment of X-ray diffraction instruments for residual stress measurement. American Society for Testing and Materials
39. Pouraliakbar H, Beygi R, Fallah V, Hosseini Monazzah A, Jandaghi MR, Khalaj G, da Silva LFM, Pavese M (2022) Processing of Al-Cu-Mg alloy by FSSP: parametric analysis and the effect of cooling environment on microstructure evolution. *Materials Letters* 308:131157
40. Mofarreh M, Javidani M, Chen XG (2022) Effect of Mn content on the hot deformation behavior and microstructure evolution of Al-Mg-Mn 5xxx alloys. *Mater Sci Eng, A* 845:143217
41. Summers PT, Chen Y, Rippe CM, Allen B, Mouritz AP, Case SW, Lattimer BY (2015) Overview of aluminum alloy mechanical properties during and after fires. *Fire Sci Rev* 4:3
42. Humphreys FJ, Hatherly M (2012) Recrystallization and related annealing phenomena. Elsevier
43. Chang CI, Lee CJ, Huang JC (2004) Relationship between grain size and Zener-Holloman parameter during friction stir processing in AZ31 Mg alloys. *Scripta Mater* 51(6):509–514
44. Nadammal N, Kailas SV, Szpunar J, Suwas S (2018) Development of microstructure and texture during single and multiple pass friction stir processing of a strain hardenable aluminium alloy. *Mater Charact* 140:134–146
45. Liu F, Xue P, Ma Z (2012) Microstructural evolution in recrystallized and unrecrystallized Al-Mg-Sc alloys during superplastic deformation. *Mater Sci Eng, A* 547:55–63
46. Dickson M (1969) The significance of texture parameters in phase analysis by X-ray diffraction. *J Appl Crystallogr* 2:176–180
47. Motavallian P, Rabiee SM, Jamshidi Aval H (2023) The microstructure and mechanical and corrosion properties of Mg matrix composites reinforced with bioactive glass: the combined effect of bioactive glass content and extrusion speed. *Mater Chem Phys* 307:128135
48. Qiu Y, Yang X, Li J, Xiang S, Shi J, Xu J, Sanders RE (2022) The influence of Sc and Zr additions on microstructure and corrosion behavior of AA5182 alloy sheet. *Corros Sci* 199:110181
49. Qiu Y, Yang X, Xu J, Li J, Xiang S, Chen Z, Sanders RE Jr (2022) Enhanced mechanical property and corrosion resistance of alloy 5182 FSW joints by Sc and Zr alloying. *Mater Charact* 194:112412
50. Foley DL, Leff AC, Lang AC, Taheri ML (2020) Evolution of  $\beta$ -phase precipitates in an aluminum-magnesium alloy at the nanoscale. *Acta Mater* 185:279–286
51. Zhang L, Liu CY, Xie HY (2022) Hall-Petch relation and grain boundary slipping in AlMgSc alloys with fine equiaxed grain structure. *Mater Charact* 194:112472
52. Huskins EL, Cao B, Ramesh KT (2010) Strengthening mechanisms in an Al-Mg alloy. *Mater Sci Eng, A* 527:1292–1298
53. Vicharapu B, Liu H, Fujii H, Narasaki K, Ma N, De A (2020) Probing residual stresses in stationary shoulder friction stir welding process. *J Adv Manuf Technol* 106:1573–1586
54. Inoue T, Wang Z (1985) Coupling between stress, temperature, and metallic structures during processes involving phase transformations. *Mater Sci Technol* 1:845–850
55. Jamshidi Aval H, Serajzadeh S, Sakharova NA, Kokabi AH, Loureiro A (2012) A study on microstructures and residual stress distributions in dissimilar friction-stir welding of AA5086-AA6061. *J Mater Sci* 47:5428–5437
56. Jamshidi Aval H, Serajzadeh S, Kokabi AH (2012) Experimental and theoretical evaluations of thermal histories and residual stresses in dissimilar friction stir welding of AA5086-AA6061. *Int J Adv Manuf Technol* 61:149–160



57. Han W, Wan F, Li G, Dong C, Tong J (2011) Effect of trailing heat sink on residual stresses and welding distortion in friction stir welding Al sheets. *Sci Technol Weld Joining* 16:453–458
58. James M, Hughes D, Hattingh D, Bradley G, Mills G, Webster P (2004) Synchrotron diffraction measurement of residual stresses in friction stir welded 5383–H321 aluminium butt joints and their modification by fatigue cycling. *Fatigue Fract Eng Mater Struct* 27:187–202
59. Deplus K, Simar A, Haver WV, B.d. Meester, (2011) Residual stresses in aluminium alloy friction stir welds. *Int J Adv Manuf Technol* 56:493–504
60. Kumar N, Mishra RS, Baumann JA (2013) Residual stresses in friction stir welding. *Butterworth-Heinemann*
61. Jamshidi Aval H (2015) Microstructure and residual stress distributions in friction stir welding of dissimilar aluminium alloys. *Mater Des* 87:405–413
62. Bararpour SM, Jamshidi Aval H, Jamaati R (2020) An experimental and theoretical investigation of thermo-mechanical issues in friction surfacing of Al-Mg aluminum alloys: material flow and residual stress. *Model Simul Mater Sci Eng* 28(3):035003
63. Mehdizade M, Eivani AR, Soltanieh M (2020) Effects of reduced surface grain structure and improved particle distribution on pitting corrosion of AA6063 aluminum alloy. *J Alloy Compd* 838:155464
64. Xu DK, Birbilis N, Lashansky D, Rometsch PA, Muddle BC (2011) Effect of solution treatment on the corrosion behaviour of aluminium alloy AA7150: optimisation for corrosion resistance. *Corros Sci* 53(1):217–225
65. Culliton D, Betts AJ, Kennedy D (2013) Impact of intermetallic precipitates on the tribological and/or corrosion performance of cast aluminium alloys: a short review. *Int J Cast Met Res* 26(2):65–71
66. Enikeev NA, Shamardin VK, Radiguet B (2019) Radiation tolerance of ultrafine-grained materials fabricated by severe plastic deformation. *Mater Trans* 60:1723–1731
67. Skiba J, Kossakowska J, Kulczyk M, Pachla W, Przybysz S, Smalc-Koziorowska J, Przybysz M (2023) The impact of severe plastic deformations obtained by hydrostatic extrusion on the machinability of ultrafine-grained AA5083 alloy. *J Manuf Process* 58:1232–1240
68. Miyamoto H (2016) Corrosion of ultrafine grained materials by severe plastic deformation, an overview. *Mater Trans* 57(5):559–572
69. Bai L, Jiang K, Gao L (2018) The influence and mechanism of residual stress on the corrosion behavior of welded structures. *Mater Res* 21(5):e20180166
70. Hatamleh O, Singh PM, Garmestani H (2009) Stress corrosion cracking behavior of peened friction stir welded 2195 aluminum alloy joints. *J Mater Eng Perform* 18(4):406–413
71. McMahon M, Harris Z, Scully J, Burns J (2019) The effect of electrode potential on stress corrosion cracking in highly sensitized Al-Mg alloys. *Mater Sci Eng, A* 767:138399

**Publisher's Note** Springer Nature remains neutral with regard to jurisdictional claims in published maps and institutional affiliations.

Springer Nature or its licensor (e.g. a society or other partner) holds exclusive rights to this article under a publishing agreement with the author(s) or other rightsholder(s); author self-archiving of the accepted manuscript version of this article is solely governed by the terms of such publishing agreement and applicable law.